



Universidad Autónoma
de Madrid

Biblos-e Archivo
Repositorio Institucional UAM

Repositorio Institucional de la Universidad Autónoma de Madrid

<https://repositorio.uam.es>

Esta es la **versión de autor** del artículo publicado en:
This is an **author produced version** of a paper published in:

Angewandte Chemie - International Edition 55.46 (2016): 14345-14349

DOI: <https://doi.org/10.1002/anie.201605298>

Copyright: © 2016 The Authors. Published by Wiley-VCH Verlag GmbH & Co. KGaA.

El acceso a la versión del editor puede requerir la suscripción del recurso

Access to the published version may require subscription

Few-Layer Antimonene by Liquid-Phase Exfoliation

Carlos Gibaja¹, David Rodriguez-San-Miguel^{1,2}, Pablo Ares³, Julio Gómez-Herrero^{3,4}, Maria Varela⁵, Roland Gillen⁶, Janina Maultzsch⁶, Frank Hauke⁷, Andreas Hirsch⁷, Gonzalo Abellán^{7*}, and Félix Zamora^{1,2,4*}

¹Departamento de Química Inorgánica, Universidad Autónoma de Madrid, 28049, Madrid (Spain)

²Instituto Madrileño de Estudios Avanzados en Nanociencia (IMDEA Nanociencia), Cantoblanco, 28049 Madrid (Spain)

³Departamento de Física de la Materia Condensada, Universidad Autónoma de Madrid, 28049 Madrid (Spain)

⁴Condensed Matter Physics Center (IFIMAC), Universidad Autónoma de Madrid, 28049 Madrid (Spain)

⁵Facultad de CC. Físicas & Instituto Pluridisciplinar, Universidad Complutense de Madrid, 28040, Madrid (Spain)

⁶Institut für Festkörperphysik, Technische Universität Berlin, Hardenbergstrasse 36, 10623, Berlin (Germany)

⁷Department of Chemistry and Pharmacy, University Erlangen-Nürnberg, Henkestrasse 42, 91054, Erlangen (Germany) and Institute of Advanced Materials and Processes (ZMP), Dr.-Mack-Strasse 81, 90762, Fürth (Germany)

E-mail: gonzalo.abellan@fau.de, E-mail: felix.zamora@uam.es

Abstract: We report on a fast and simple method to produce highly stable isopropanol/water (4:1) suspensions of few-layer antimonene by liquid-phase exfoliation of antimony crystals in a process that is assisted by sonication but does not require the addition of any surfactant. This straightforward method generates dispersions of few-layer antimonene suitable for on-surface isolation. Analysis by atomic force microscopy, scanning transmission electron microscopy, and electron energy loss spectroscopy confirmed the formation of high quality few-layer antimonene nanosheets with large lateral dimensions. These nanolayers are extremely stable under ambient conditions. Their Raman signals are strongly thickness-dependent, which was rationalized by means of density functional theory calculations.

Currently, two-dimensional (2D) materials represent one of the most active research areas.^[1] Apart from various well-established 2D materials, such as graphene, h-BN, and MoS₂, black phosphorus (BP) has received considerable attention over the last two years.^[2] This is due to the fact that whereas graphene is a non-band-gap material and transition-metal dichalcogenides have a relatively large band gap for certain optoelectronic applications (1.5–2.5 eV),^[3] the direct band gap of few- and single-layer BP is approximately 1.5 eV,^[4] and this material therefore has appealing properties for electronic and ultrafast optoelectronic applications. However, isolated layers of BP are extremely sensitive to the surroundings, and strongly degrade upon air exposure, which limits their application.^[2b] Thus the discovery of new 2D materials with an appropriate band gap and stability under ambient conditions is a challenge of utmost importance.

Along this front, antimony is a good candidate as it is in the same group in the periodic table as phosphorus and exhibits an allotrope closely related to BP (Figure 1a). Indeed, theoretical calculations^[5] have estimated the band gap for a single layer of antimony, or antimonene (we should point out that the name antimonene is not completely correct as there are no double bonds in its structure), to be about 1.2 eV. Antimonene has recently been isolated by mechanical exfoliation, and showed good stability under ambient conditions.^[6] As for other 2D materials, micromechanical exfoliation provides high-quality flakes but is unsuitable for mass production. Liquid phase exfoliation (LPE) has been successfully applied to generate single-

or few-layer (FL) samples of several 2D materials on large scale,^[7] including stable suspensions of few-layer BP.^[8]

Herein, we demonstrate that sonication of antimony crystals in a 4:1 isopropanol/water mixture without any surfactant produces a very stable suspension of micrometerlarge FL antimonene over weeks, even under ambient conditions (see the Supporting Information for details). High-quality, few-layer antimonene nanosheets can thus be produced by liquid-phase exfoliation. Remarkably, the FL antimonene suspensions and the layers isolated on surfaces are very stable, even for weeks, under ambient conditions.

LPE of antimony crystals (see Figure 1a for their structure) was carried out by sonication of ground antimony crystals (see Figure 1b for a scanning electron microscopy (SEM) image) in 4:1 iPrOH/water for 40 min at 400 W and 24 kHz, which yielded a colorless dispersion (Figure 1c), showing the Faraday–Tyndall effect. Non-exfoliated material was removed by centrifugation at 3000 rpm (845 rcf) for 3 min to produce a stable dispersion with a concentration of about $1.74 \times 10^{-3} \text{ gL}^{-1}$, as determined by atomic absorption spectroscopy (see the Supporting Information for a detailed analysis of the preparation conditions as well as information concerning solvent selection, optimization of the experimental exfoliation, centrifugation parameters, and UV/Vis spectroscopy).

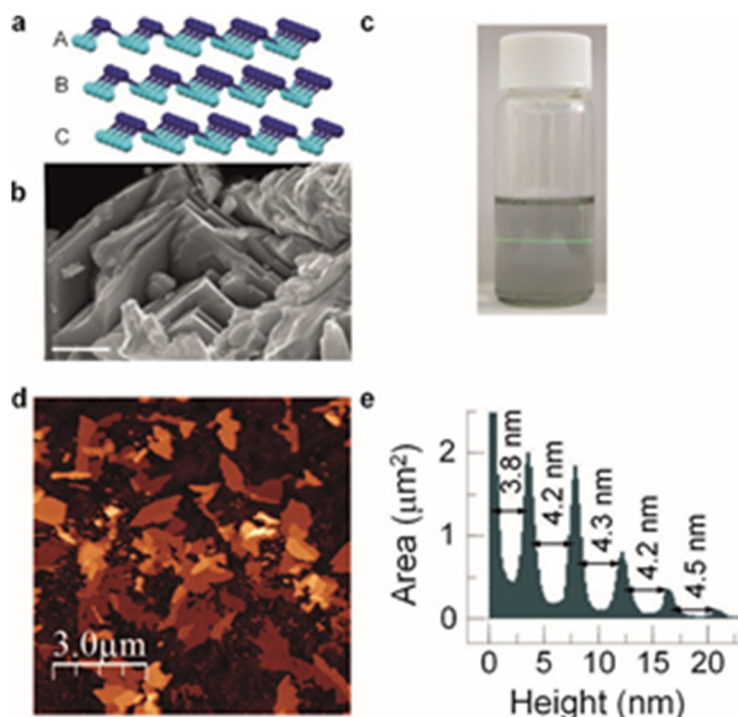


Figure 1. a) Structure of β -antimonene. b) SEM image of a layered antimony crystal (scale bar: 1 μm). c) Photograph of a dispersion of exfoliated FL antimonene showing the Faraday–Tyndall effect. d) Topographic AFM image of few-layer antimonene drop-casted onto SiO_2 showing flakes with micrometer lateral dimensions (scale bar: 3 μm). e) Height histogram of the image in (d) where the different thicknesses of the terraces can be readily seen. For the sake of clarity, the substrate peak has been cut to 2.5 μm^2 . The constant minimum thickness of about 4 nm can be easily observed.

Exfoliation of the antimony crystals was readily confirmed by atomic force microscopy (AFM). Figure 1d shows a characteristic topographic image of FL antimonene flakes isolated on SiO_2 substrates (see the Supporting Information, Figure S6 for more AFM images). As reflected in the height histogram of the image (Figure 1e), the step heights are multiples of

about 4 nm. Furthermore, the flakes do not show the typical terrace characteristics of layered materials but well-defined structures with all heights being multiples of about 4 nm (Figures 1d,e, 2b, and S7). As it is well-known that the apparent AFM heights of layers obtained by LPE can be overestimated because of residual solvent^[8,9] as well as contributions from effects such as capillary and adhesion forces,^[10] it seems likely that the apparent mono/bilayer thickness is about 4 nm. The overall lateral dimensions of the isolated nanosheets are greater than 1–3 μm^2 (see Figure S4 for a statistical analysis). Transmission electron microscopy (TEM) measurements further confirmed the success of the exfoliation (Figure S11).

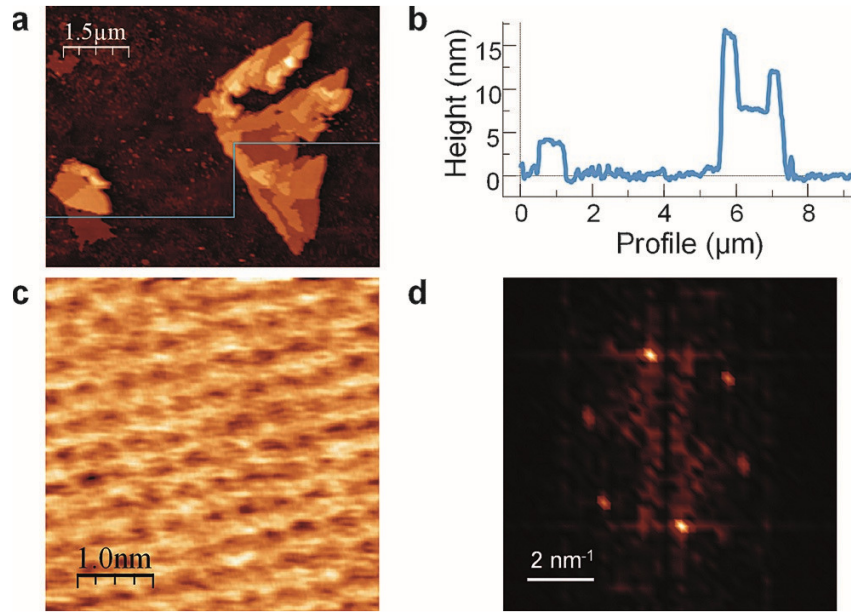


Figure 2. a) AFM topography showing several FL antimonene flakes with terraces of different heights. b) Height profile along the horizontal line of the image in (a) where the different thicknesses of the terraces can be readily seen. The minimum step height is about 4.0 nm. c) AFM image showing the atom periodicity. d) Fast Fourier transform (FFT) image taken from (c), showing the agreement with a hexagonal lattice as expected for β -antimony.

A high-resolution AFM topographic image taken of the lowest terrace (ca. 4 nm) of the isolated flake shown in Figure 2a exhibits an atomic periodicity in line with that expected for β -antimony (Figure 2c). To obtain insight into the stability of the nanosheets, atomic periodicity images were taken after exposing the flake to atmospheric conditions for more than two weeks, which confirmed the outstanding stability of few-layer antimonene under these ambient conditions (Figure S8).

Moreover, the Fourier transforms obtained from the AFM topographic images revealed hexagonal symmetry as expected for β -antimony, indicating excellent crystal quality. This finding is consistent with the results of other real-space techniques with atomic resolution (Figure S11). Aberration corrected scanning transmission electron microscopy (STEM) combined with electron energy loss spectroscopy (EELS) was used to investigate the local structure and chemistry of the flakes. Figure 3a shows a low-magnification high angle annular dark field (HAADF) image of a flake (top left) along with an atomic-resolution image of the crystal structure, both obtained at an acceleration voltage of 80 kV to prevent beam-induced damage. This structure (Figure 3a) agrees with that of β -antimony along the [0 -1 2] direction. The samples were crystalline, and no major defects were observed. Compositional maps were obtained from the EEL spectra including the C K, Ca L_{2,3}, O K, and Sb M_{4,5} absorption edges.

Whereas little chemical inhomogeneity was detected within the flakes, the flake ends appeared to be somewhat damaged. A series of such maps from areas near the edges are shown in Figures 3b and S8. Whereas a homogeneously distributed Sb signal was observed, a significant C signal was present within a few nanometers of the sample edge, pointing to some degree of surface contamination. Similarly, traces of O and Ca were detected within tens of nanometers from the edges, which is very likely due to the same reason (Ca is present because of solvent contamination).

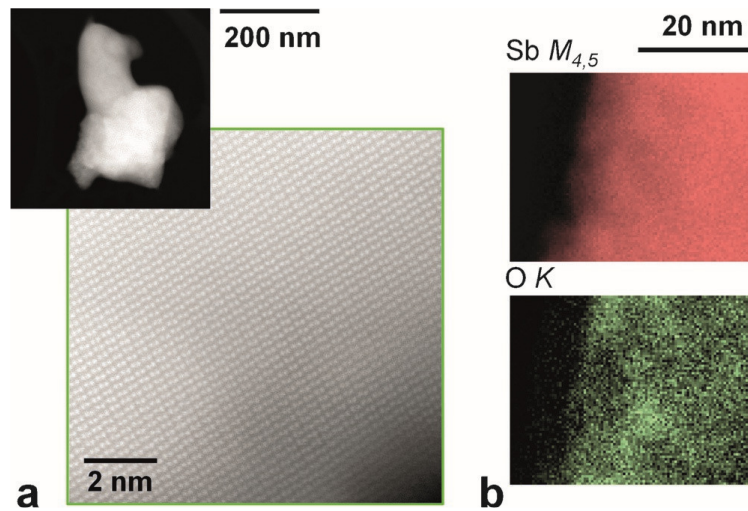


Figure 3. a) Low-magnification HAADF image of a flake (top left) along with an atomic-resolution image (image taken along the [0 -1 2] direction). b) Two-dimensional EELS maps acquired near the edge of the flake, showing the signals below the Sb $M_{4,5}$ (red) and O K (green) absorption edges.

Raman spectroscopy is a powerful method commonly used for the characterization of 2D materials. The Raman spectrum of bulk antimony when excited off resonance ($\lambda = 532$ nm) exhibits two main phonon peaks (the A_{1g} mode at 149.8 cm^{-1} and E_g mode at 110 cm^{-1}).^[11] Correlation of AFM and statistical Raman microscopy (SRM)^[12] in a polydisperse sample revealed that flakes with an apparent thickness below about 70 nm (ca. 17 layers) hardly show any measurable Raman signal (Figure 4b). This unexpected dependence of the Raman intensity on the flake thickness is similar to that previously observed for micromechanically exfoliated flakes of antimony and analogous to what has been reported for mica nanosheets.^[6,13] Indeed, Figure 4b shows a series of single-point spectra measured at different positions, showing decreases in the peak intensities with a decrease in thickness. For comparison, we studied the influence of the laser excitation wavelength on a micromechanically exfoliated flake with a size of about $5.5\text{ }\mu\text{m}$ and a thickness of 10 nm, which had previously been analyzed by AFM, after its relocation in a Raman microscope by optical microscopy (see the Supporting Information and Figure S13 for additional information). As expected for this thickness, no Raman signal was detected, even after increasing the acquisition time and using different laser excitation wavelengths ($\lambda_{\text{ex}} = 785, 633, 532, 473, 457$, and 405 nm; Figure S11). However, the thinner flakes can be clearly located by SRM by monitoring the decrease in the silicon characteristic peak at about 521 cm^{-1} (Figure S15).

To complement our experimental results, we calculated the theoretical phonon spectra of bulk and few-layer antimony. We thus modeled the b-phase of bulk Sb, which consists of buckled quasi-2D layers of Sb in an ABC-type sequence (space group $\bar{R}3m$). For the primitive cell with rhombohedral axes and two atoms, this structure yields three optical modes, which are all Raman active: A pair of degenerate modes of E_g symmetry, which corresponds to the

in-plane transversal and longitudinal vibrations of the sublayers in opposite directions, gives rise to the experimentally observed Raman peak at 100 cm^{-1} . The peak at 150 cm^{-1} is caused by the third mode, opposite-in-phase out-of-plane vibrations of the sublayers of A_{1g} symmetry. Our calculations underestimated both frequencies by about 9%, and we obtained values of 88 and 137 cm^{-1} . This softening of the optical phonons in DFT calculations has been observed before,^[14] and appears to be related to the strong electron–lattice interaction and the negative Grüneisen parameter in antimony^[11] and similar materials, such as bismuth.

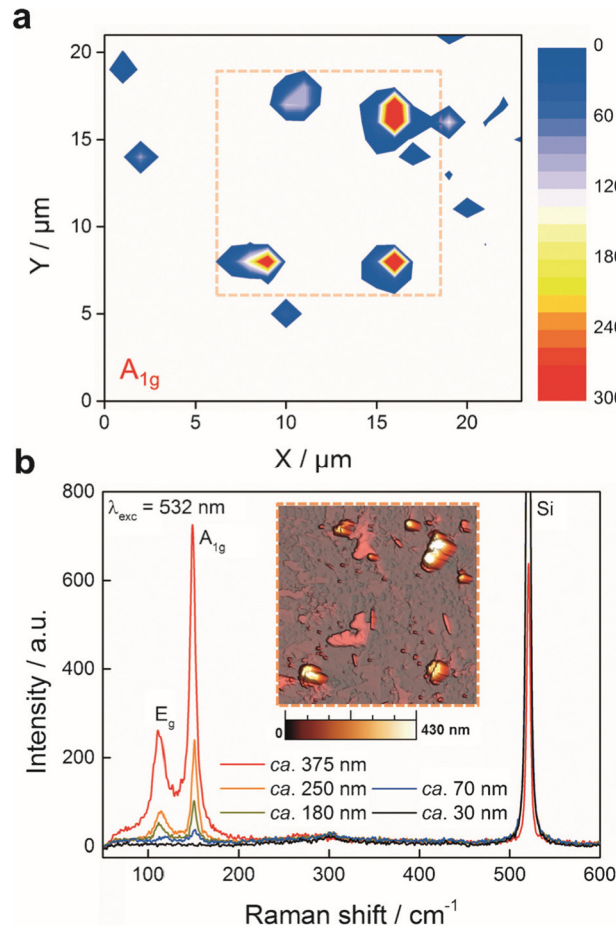


Figure 4. a) A_{1g} intensity Raman mapping of solvent-exfoliated flakes deposited on a SiO_2/Si substrate, showing the presence of several flakes. b) Single-point spectra measured at different thicknesses according to the topographic AFM image (inset) of the same area studied in (a). The dashed square corresponds to the position of the AFM image shown in (b).

For the few-layer system, our calculations predict a strong contraction of the in-plane lattice constant compared to the bulk material ($a = 4.3\text{ \AA}$) when the film thickness is decreased to a trilayer ($a = 4.19\text{ \AA}$), bilayer ($a = 4.15\text{ \AA}$), and monolayer ($a = 4.01\text{ \AA}$). As a result, the frequency of the bulk E_g mode gradually increases from 88 to 167 cm^{-1} in monolayer Sb. In a similar fashion, the bulk A_{1g} mode is blue-shifted with a decrease in film thickness, although to a smaller extent owing to the lower sensitivity of the out-of-plane modes to the in-plane lattice constant. In fact, the frequency increased from 137 cm^{-1} in the bulk to 208 cm^{-1} for the monolayer (1L) system. Interestingly, in the bilayer (2L) case, the frequencies of the E_u and A_{2u} modes are higher than those of the corresponding E_g and A_{1g} modes. This seems counterintuitive as the sublayers oscillate in phase with their counterparts in the other layers for the E_u and A_{1g} modes (see the atomic displacement patterns in Figure 5). As a result, the intra-layer bond lengths do not change and should thus not contribute to the excitation energy

of the vibration. However, it is possible that the Raman active E_g and A_{1g} modes benefit from energy compensation compared to the E_u and A_{2u} modes, for example, through strengthening of the weak covalent interlayer bonds through periodic expansion and contraction. We observed a similar effect for the trilayer system.

We also calculated the non-resonant Raman intensities for the monolayer and bulk systems (Figure 5c).^[15] Within the applied approximations, our calculations suggest a strong influence of the thickness on the simulated Raman activity, which decreases by about three orders of magnitude from bulk to monolayer Sb, which explains the experimentally observed absence of Raman signals in the thinnest flakes (Figure 4b). This behavior is in stark contrast to that of BN, for example, where the dependence of the predicted Raman tensor on the layer number is weak. It is thus possible that the experimentally observed suppression of Raman activity in Figure 4b for samples of sub-micrometer thickness has a contribution from a qualitative change in light–phonon coupling that is due to the decreasing layer number. We believe that this hypothesis warrants further investigation (see the Supporting Information for computational details and Tables with lattice constants and calculated frequencies).

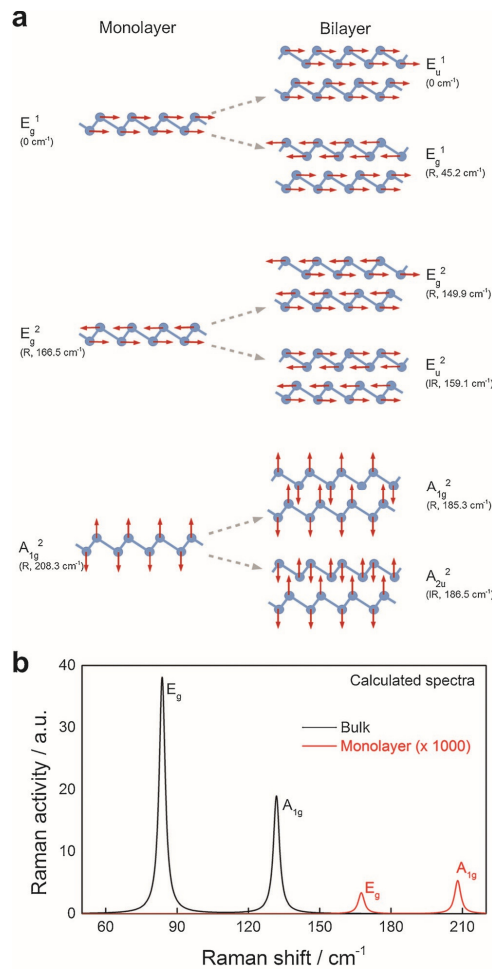


Figure 5. a) Atomic displacement patterns for the G point phonon modes in monolayer antimony (left) and the corresponding vibrations in the bilayer material (right). The E_g and E_u modes are doubly degenerate, and each mode has a partner mode (not shown) of the same frequency, with atoms vibrating perpendicularly to the plane of the paper. The out-of-plane acoustic A_{2u}^1 mode in monolayer Sb gives rise to two additional modes in the bilayer structure, the acoustic A_{2u}^1 and the optical A_{1g}^1 mode (both not shown). The calculated frequencies and Raman (R) or infrared (IR) activity are indicated in parentheses. b) Calculated Raman spectra for bulk antimony and single-layer antimonene. According to the experimental observations, the Raman signals for a monolayer are of very low intensity (>1000 times less Raman active than for the bulk counterpart), precluding its detection.

The Raman results suggest that the isolated antimony nanosheets clearly consist of only few layers, as no Raman signal was observed for nanosheets with an AFM height of 30 nm. This implies that these nanosheets have a thickness of about 60 layers, assuming a theoretical thickness of about 0.5 nm for the antimony layers. In view of the theoretical calculations and experiments, it seems very unlikely to observe an impact on Raman spectra for nanosheets with a thickness over 60 layers. The Raman analysis therefore suggests that the apparent AFM thickness of about 4 nm could correspond to a single layer or bilayer of antimony.

In summary, we have reported on a procedure to generate very stable suspensions of high-quality single/few-layer antimonene. Moreover, we have described the thickness-dependent Raman behavior of antimonene, defining the most important fingerprints for its Raman spectroscopic analysis. The scalable and environmentally friendly approach for isolating few-layer antimonene in aqueous solution will pave the way for the development of new antimonene-based technologies.

Acknowledgements

We thank MINECO (Spain) for financial support through the “María de Maeztu” Programme for Units of Excellence in R&D (MDM-2014-0377) and the projects CSD2010-0024, MAT2013-46753-C2-1-P, and -2-P as well as MAT2015-66888C3-3-R. Co-funding from UE is also acknowledged. The research leading to these results has received partial funding from the European Union Qs Seventh Framework Programme (604391, “Graphene Flagship”). Financial support from the Fundaciln BBVA is gratefully acknowledged. Electron microscopy studies were carried out at the Centro Nacional de Microscopía Electrónica, Universidad Complutense de Madrid. We thank J. Garcia for support with the TEM measurements. The computation resources used for the simulations in this work were provided by the NorthGerman Supercomputing Alliance (HLRN, bep00047). J.M. gratefully acknowledges support by the European Research Council (ERC, 259286) and by the SPP 1459 “Graphene” of the DFG. G.A. thanks the EU for a Marie Curie Fellowship (FP7/2013-IEF-627386).

References

- [1] a) Q. Tang, Z. Zhou, *Prog. Mater. Sci.* 2013, 58, 1244–1315; b) Q. Tang, Z. Zhou, Z. F. Chen, *Wires Comput. Mol. Sci.* 2015, 5, 360– 379; c) R. Mas-Ballest, C. Gomez-Navarro, J. Gomez-Herrero, F. Zamora, *Nanoscale* 2011, 3, 20–30; d) A. K. Geim, *Science* 2009, 324, 1530–1534; e) K. S. Novoselov, V. I. Fal'ko, L. Colombo, P. R. Gellert, M. G. Schwab, K. Kim, *Nature* 2012, 490, 192–200; f) A. C. Ferrari et al., *Nanoscale* 2015, 7, 4598– 4810; g) M. Chhowalla, H. S. Shin, G. Eda, L. J. Li, K. P. Loh, H. Zhang, *Nat. Chem.* 2013, 5, 263–275; h) Q. Wang, D. O'Hare, *Chem. Rev.* 2012, 112, 4124–4155.
- [2] a) A. Castellanos-Gomez, *J. Phys. Chem. Lett.* 2015, 6, 4873– 4873; b) X. Ling, H. Wang, S. X. Huang, F. N. Xia, M. S. Dresselhaus, *Proc. Natl. Acad. Sci. USA* 2015, 112, 4523–4530.
- [3] Q. H. Wang, K. Kalantar-Zadeh, A. Kis, J. N. Coleman, M. S. Strano, *Nat. Nanotechnol.* 2012, 7, 699–712.
- [4] C. Tan, H. Zhang, *Chem. Soc. Rev.* 2015, 44, 2713–2731.
- [5] a) S. Zhang, Z. Yan, Y. Li, Z. Chen, H. Zeng, *Angew. Chem. Int. Ed.* 2015, 54, 3112–3115; *Angew. Chem.* 2015, 127, 3155–3158; b) O. 3. Aktürk, V. O. Özçelik, S. Ciraci, *Phys. Rev. B* 2015, 91, 235446.
- [6] P. Ares, F. Aguilar-Galindo, D. Rodríguez-San-Miguel, D. A. Aldave, S. D&az-Tendero, M. Alcam&, F. Mart&n, J. Gómez-Herrero, F. Zamora, *Adv. Mater.* 2016, 28, 6332–6336.

- [7] a) V. Nicolosi, M. Chhowalla, M. G. Kanatzidis, M. S. Strano, J. N. Coleman, *Science* 2013, 340, 1226419; b) J. N. Coleman, *Acc. Chem. Res.* 2013, 46, 14–22.
- [8] D. Hanlon, C. Backes, E. Doherty, C. S. Cucinotta, N. C. Berner, C. Boland, K. Lee, A. Harvey, P. Lynch, Z. Gholamvand, S. F. Zhang, K. P. Wang, G. Moynihan, A. Pokle, Q. M. Ramasse, N. McEvoy, W. J. Blau, J. Wang, G. Abellan, F. Hauke, A. Hirsch, S. Sanvito, D. D. OQRegan, G. S. Duesberg, V. Nicolosi, J. N. Coleman, *Nat. Commun.* 2015, 6, 8563.
- [9] K. R. Paton, E. Varrla, C. Backes, R. J. Smith, U. Khan, A. OQNeill, C. Boland, M. Lotya, O. M. Istrate, P. King, T. Higgins, S. Barwich, P. May, P. Puczkarski, I. Ahmed, M. Moebius, H. Pettersson, E. Long, J. Coelho, S. E. OQBrien, E. K. McGuire, B. M. Sanchez, G. S. Duesberg, N. McEvoy, T. J. Pennycook, C. Downing, A. Crossley, V. Nicolosi, J. N. Coleman, *Nat. Mater.* 2014, 13, 624–630.
- [10] P. Nemes-Incze, Z. Osvath, K. Kamaras, L. P. Biro, *Carbon* 2008, 46, 1435–1442.
- [11] X. Wang, K. Kunc, I. Loa, U. Schwarz, K. Syassen, *Phys. Rev. B* 2006, 74, 134305.
- [12] a) F. Hof, S. Bosch, J. M. Englert, F. Hauke, A. Hirsch, *Angew. Chem. Int. Ed.* 2012, 51, 11727–11730; *Angew. Chem.* 2012, 124, 11897–11900; b) J. M. Englert, P. Vecera, K. C. Knirsch, R. A. Schfer, F. Hauke, A. Hirsch, *ACS Nano* 2013, 7, 5472–5482.
- [13] A. Castellanos-Gomez, M. Wojtaszek, N. Tombros, N. Agrait, B. J. van Wees, G. Rubio-Bollinger, *Small* 2011, 7, 2491–2497.
- [14] D. Campi, M. Bernasconi, G. Benedek, *Phys. Rev. B* 2012, 86, 075446.
- [15] D. Porezag, M. R. Pederson, *Phys. Rev. B* 1996, 54, 7830–7836.

Supporting Information

1. Materials and Methods

Commercially available antimony material (99.9999%, Smart Elements), deionized Millipore Milli-Q water ($R > 18.2 \text{ M}\Omega$) and 2-propanol (99.8 %, Panreac) were used.

Atomic Force Microscopy (AFM) imaging: AFM measurements were carried out using a Cervantes Fullmode AFM from Nanotec Electronica SL. WSxM software (www.wsxmsolutions.com) was employed both for data acquisition and image processing.^[1] All the topographical images shown in this work were acquired in contact mode to avoid possible artefacts in the flake thickness measurements.^[2] OMCL-RC800PSA cantilevers (probe.olympus-global.com) with a nominal spring constant of 0.39 N/m and tip radius of 15 nm were employed. Low forces of the order of 1 nN were used for imaging to ensure that the flakes would not be deformed by the tip.

Surface preparation: SiO_2 surfaces were sonicated for 15 min. in acetone and 15 min. in 2-propanol and then dried under an argon flow.

Atomic Absorption Spectrometry: Antimony determination was carried out by flame atomic absorption spectrometry using a ContrAA 700 high-resolution atomic absorption spectrometer (Analytik Jena, Germany). The main line for antimony at 217.5815 nm was employed for all the analysis. The atomization was performed using an air acetylene flame with an acetylene flow rate of 60 L h^{-1} and at a 6.0 mm burner height. The aspiration rate was fixed at 5 mL min^{-1} . All measurements were carried out in triplicate.

Turbidimeter: Measurements were carried out using a HI-88713 Bench Top Turbidity Meter Hanna Instruments.

Optical absorption spectroscopy (OAS) was measured on suspensions using an Agilent 8452 diode array recorded over a 190–1100 nm range.

Transmission Electron Microscopy (TEM): Images were obtained in a JEOL JEM 2100 FX TEM system with an accelerating voltage of 200 kV. The microscope has a multiscan charge-coupled device (CCD) camera ORIUS SC1000 and an OXFORD INCA X-Ray Energy Dispersive Spectroscopy (XEDS) microanalysis system.

Scanning Transmission Electron Microscopy (STEM) combined with electron energy-loss spectroscopy (EELS): Obtained at 80 kV in a JEOL ARM200cF equipped with a spherical aberration corrector and a Gatan Quantum EEL spectrometer.

Field-Emission Scanning Electron Microscopy (FESEM): studies were performed on a Philips XL 30 S-FEG microscope operating at an accelerating voltage of 10 kV.

Raman spectroscopy: Scanning Raman Microscopy on individual flakes was performed using a Horiba Jobin Yvon LabRAM HR Evolution confocal Raman spectrometer equipped with a microscope and an automated XYZ-table (excitation wavelengths 785, 633, 532, 473, 457 and 405 nm) with a laser spot size of $1 \mu\text{m}$ (Olympus LMPlanFl 100x, NA 0.80). The incident laser power was kept as low as possible to avoid structural sample damage and the grating was $1800 \text{ g}\cdot\text{mm}^{-1}$. The spectra were recorded under

ambient conditions. Relocalization was achieved by using the optical contrast of nanomaterials deposited on opaque bilayered substrates.

Standard exfoliation procedure: 10 mg of powdered antimony were put on a 20 mL vial with 10 mL of an 4:1 2-propanol:water mixture. The mixture was sonicated for 40 min. at 400 W and 24 kHz delivering the ultrasound power in pulses 0.5 s long every 1 s. Then, the resulting black suspension was centrifuged at 3000 rpm (845 rcf) for 3 min. and the clear supernatant was recovered. 20 μ L of the suspension were casted on a SiO₂ surface and allowed to dry.

Sonicator device: Sonication was performed using a Hielscher UP400S ultrasonic processor equipped with a 3 mm sonotrode.

Centrifugation was carried out in a MPW-350R centrifuge using 2 mL Eppendorfs.

1. Determination of Experimental Exfoliation Conditions

1.1 Solvent Selection

Several pure solvents were tested in order to get liquid exfoliation of crystals of antimony. The solvents were selected based on its surface energy in order to match with the layered crystals and minimize the energy cost of the exfoliation according to the enthalpy of mixing per unit volume as shown in eq. (1),

$$\frac{\Delta H_{mix}}{V_{mix}} \approx \frac{2}{T_{layer}} (\delta_{layer} - \delta_{solvent})^2 \phi$$

eq. (1)

Where $\delta_i = \sqrt{E_{sur}^i}$ is the square root of the component surface energy, T_{layer} is the thickness of an antimonene flake and ϕ the volume fraction.^[3] The surface energy of the antimonene is still unknown. Therefore we just tried to test several solvents according to their surface tension (Table S1).

Table S1. Surface tension of the tested solvents.

Solvents	Surface tension (mN/m) 20 °C
Ethanol	22.1
2-Propanol	23.0
Acetone	25.2
Chloroform	27.5
N-methyl-2-pyrrolidone	40.8
Water	72.8

10 mg of powdered antimony in 10 mL of the solvent were sonicated for 40 min. at 400 W and 24 kHz but only sedimentation, or very little dispersion of material were observed immediately after sedimentation for 12 h (Table S2). Based in our previous results with the exfoliation of graphite^[4] we tested mixtures of organic solvents with water. Indeed, the best result was obtained with the mixture 4:1 2-propanol:water. Other tested experimental conditions are collected in Table S2 showing poor concentration of material in suspension. The concentration of antimony was estimated based on the turbidimetric measurements on the suspensions (Figure S1).

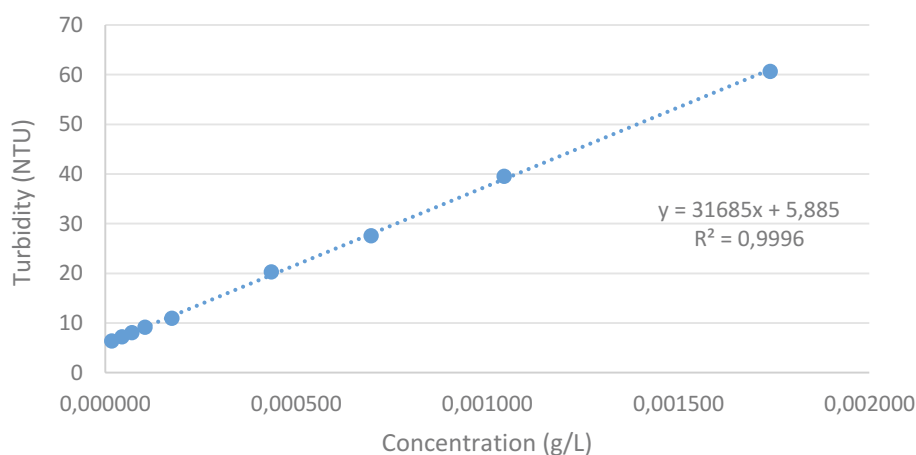


Figure S1. Calibration of the turbidity (NTU units) *versus* concentration (g/L).

Table S2. Summary of the experimental conditions tested.

Pure solvent	Turbidity (NTU)	Concentration (g/L)
2-Propanol	29.2	0.074×10^{-3}
NMP	32.9	0.085×10^{-3}
2-Propanol/H ₂ O	Turbidity (NTU)	Concentration (g/L)
(4:1)	60.7	1.74×10^{-3}
(2:1)	28.3	0.71×10^{-3}
(1:1)	23.9	0.57×10^{-3}
(1:2)	14.8	0.28×10^{-3}
H ₂ O	6.3	0.01×10^{-3}

1.2 Adjustment of the Exfoliation Experimental Setup

Once the solvent is selected, several experimental factors may affect to the liquid phase exfoliation process of a layered material to form a stable dispersion. These include the sonication time, initial quantity of the material or the centrifugation time and speed, among others.

Figure S2 shows the effect of the sonication time on the concentration. The variation in the concentration from sonication times ranging between 20 to 90 min is not very

significant. However, we have observed that larger sonication times produce a dramatic decrease in the concentration probably due to degradation.

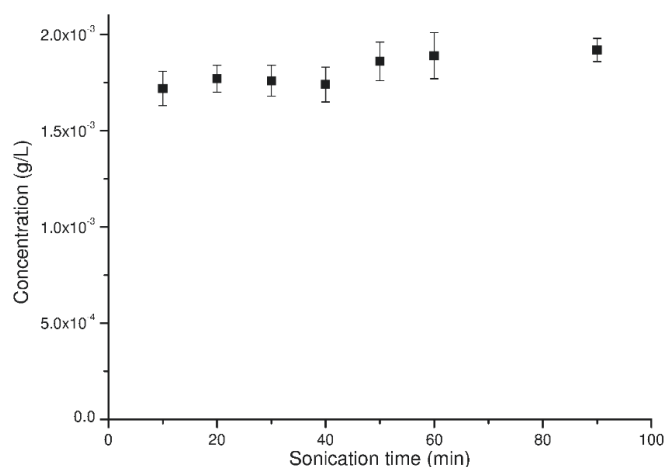


Figure S2. Study of few-layer antimonene flakes concentration (g/L) found in suspension *versus* sonication time (centrifugation after sonication was used to get a homogeneous suspension). This measure was determined by atomic absorption spectrometry.

The analysis of the effect in the final concentration of antimony in suspension based on the initial quantity of antimony in 10 mL of 2-propanol:water (4:1) is given in Table S3. It can be observed that an increase of the initial amount of antimony does not cause a significant effect on the concentration.

Table S3. Analysis of the amount of initial antimony powder dispersed in 10 mL of 2-propanol:water (4:1) and the final concentration of antimony obtained in suspension.

Initial Quantity (g)	Turbidity (NTU)	Concentration (g/L)
0.001	51.2	1.43×10 ⁻³
0.01	60.7	1.74×10 ⁻³
0.02	55.3	1.56×10 ⁻³
0.05	58.9	1.67×10 ⁻³

The optimization of the centrifugation time shows that the best results are obtained at short times (Table S4). The effect of the centrifugation process in concentration is noteworthy. Indeed further improving of centrifugation conditions is expected to lead to dispersions with controlled flake sizes in the future, but such optimization is beyond the scope of this work.

Table S4. Study of the effect of the centrifugation time on the final concentration.

Centrifugation time (min)	Turbidity (NTU)	Concentration (g/L)
3	60.7	1.74×10^{-3}
10	10.1	0.13×10^{-3}
30	6.17	0.01×10^{-3}

1.3 Stability of the Antimony Suspensions

The suspension of antimony obtained upon sonication for 40 min. at 400 W of 10 mg of powdered antimony with 10 mL of 2-propanol:water (4:1) shows good stability with the time. After 24 h only *ca.* 20 % of the initial material observed in suspension is deposited, and at long times, 72 h, an extra 10 % of the initial material is deposited.

Table S5. Stability of the antimony suspension with the time.

Time (h)	Turbidity (NTU)	Concentration (g/L)
0	60.7	1.74×10^{-3}
1	55.3	1.56×10^{-3}
2	54.9	1.55×10^{-3}
3	53.1	1.49×10^{-3}
24	50.2	1.40×10^{-3}
48	46.7	1.29×10^{-3}
72	44.4	1.22×10^{-3}
96	42.6	1.12×10^{-3}
120	41.2	1.11×10^{-3}
144	40.1	1.08×10^{-3}
168	39.3	1.05×10^{-3}

We also measured the UV-vis absorption spectra of the suspensions showing a continuous decrease of the intensity as a function of time, likely related with precipitation and/or reaggregation of the nanosheets, in good agreement with the turbidity experiments (Figure S3). All the samples exhibited a broad spectrum with no alteration of its shape, suggesting that no degradation is occurring.

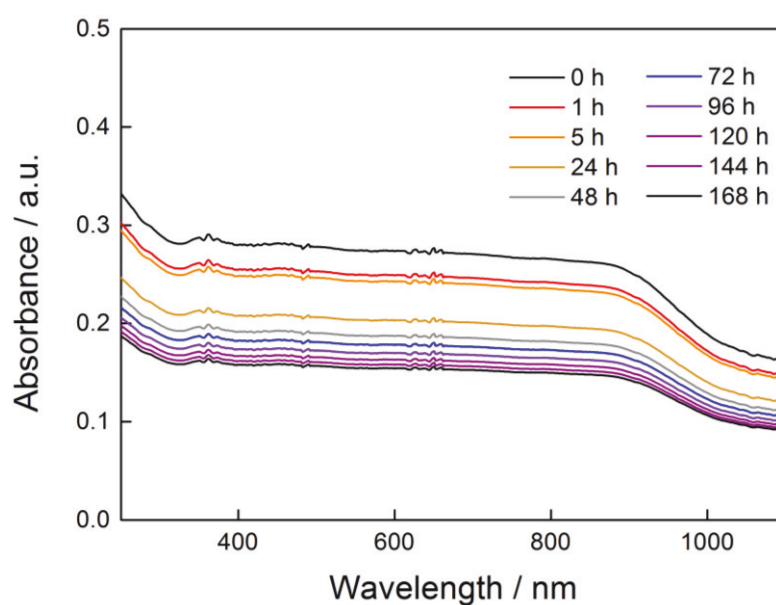


Figure S3. Absorbance spectra of few-layers antimonene suspensions as a function of time, showing a decrease in the intensity, related to the sedimentation process.

1.2 Determination of the Morphological Features

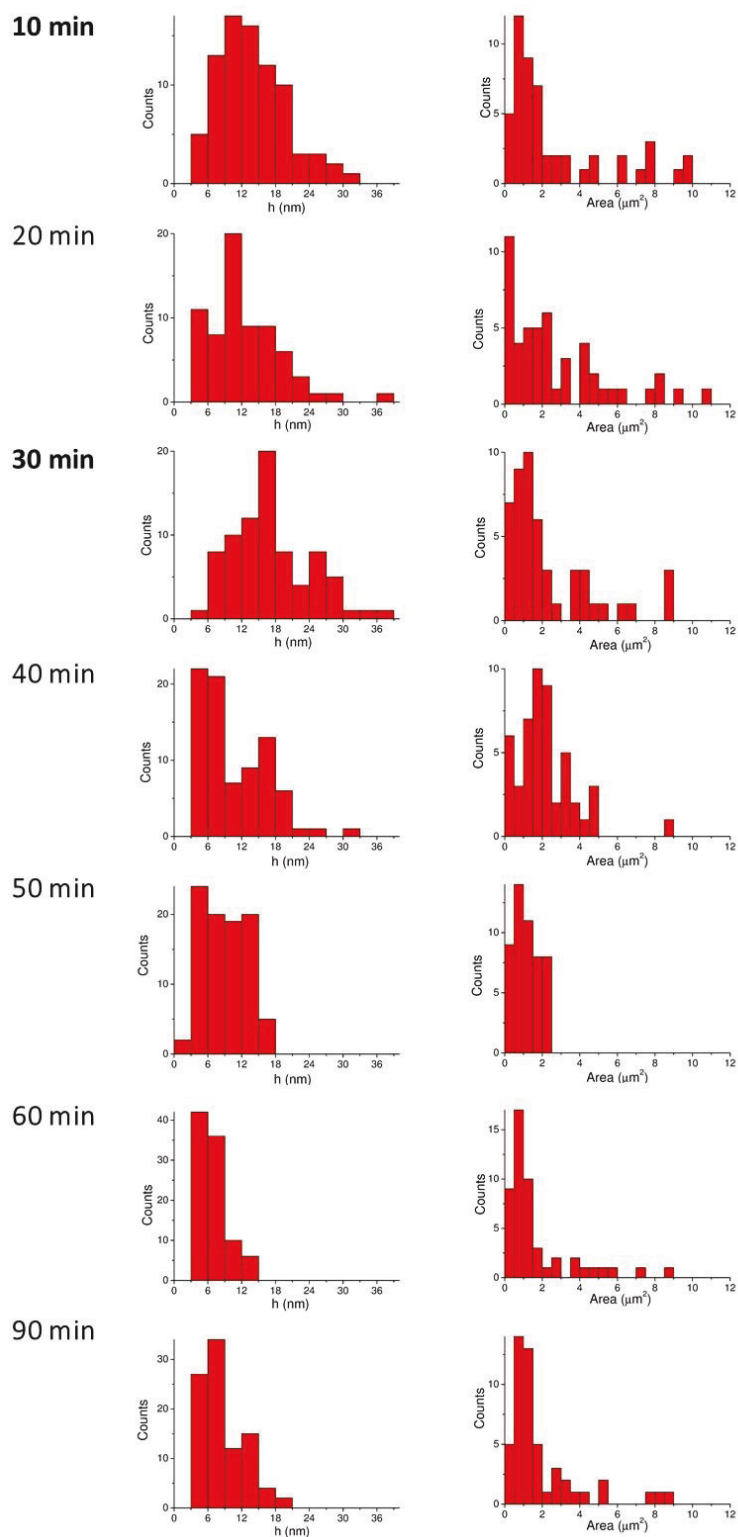


Figure S4. Representation of the height (left panels) and lateral dimension (right panels) variation of few-layer antimonene flakes *versus* sonication time. The analysis was done measuring the dimensions of the antimony layers by atomic force microscopy. Area measured using WSxM 5.0 software.^[1a]

2. Additional Characterization Data

2.1 Total reflection X-Ray Fluorescence Analysis

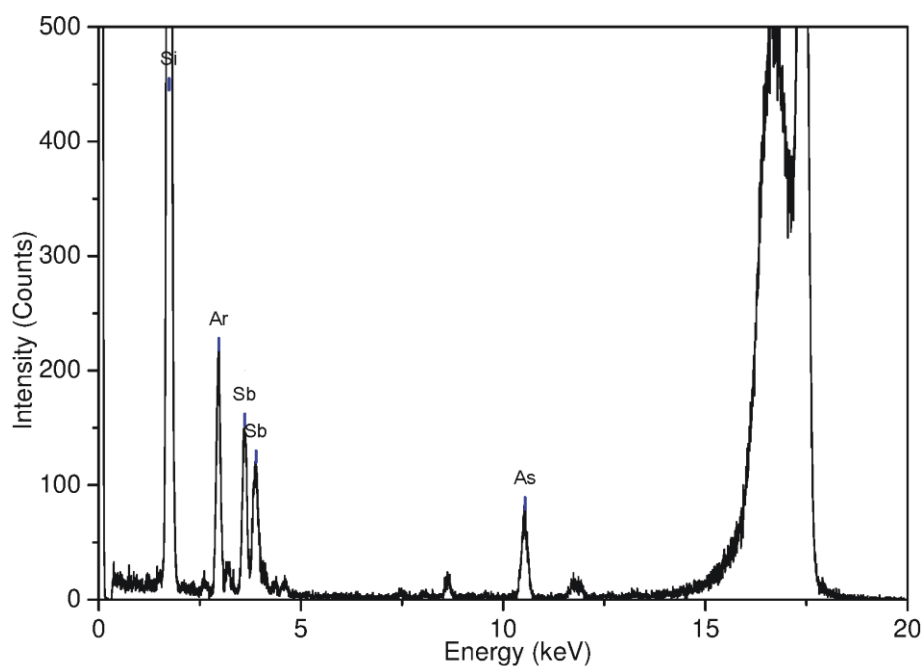


Figure S5. Total reflection X-Ray Fluorescence Spectra of a suspension of few-layer antimonene showing that it only contains antimony and some traces of arsenic (probably from impurities in the starting material). The signal of silicon comes from the sample holder, and argon from the atmosphere. The silicon peak is not completely displayed for clarity.

2.2 Atomic Force Microscopy

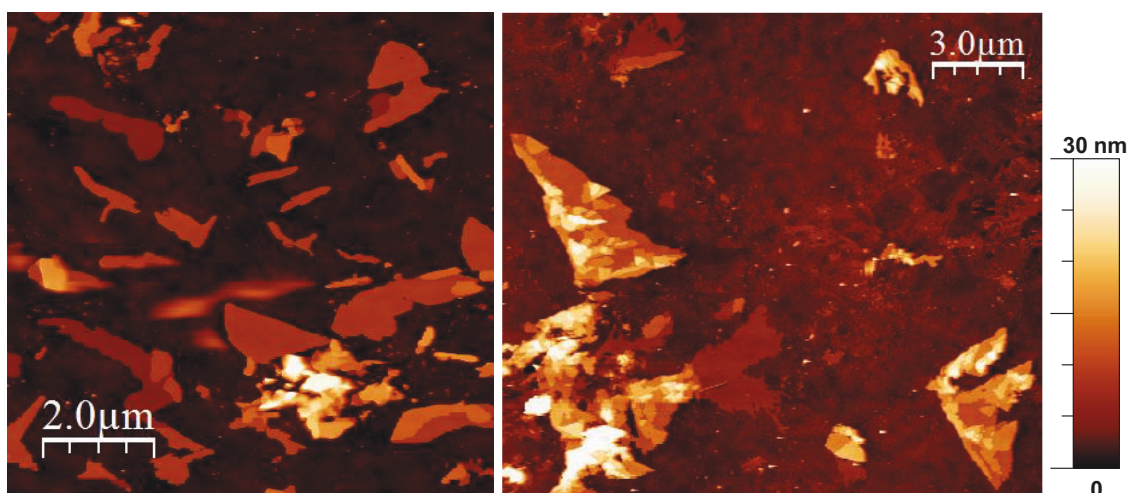


Figure S6. AFM topographic images showing different areas with few-layer antimonene flakes. Notice the angles observed in the edges of the flakes, mainly multiples of 60° , as expected for a hexagonal structure.

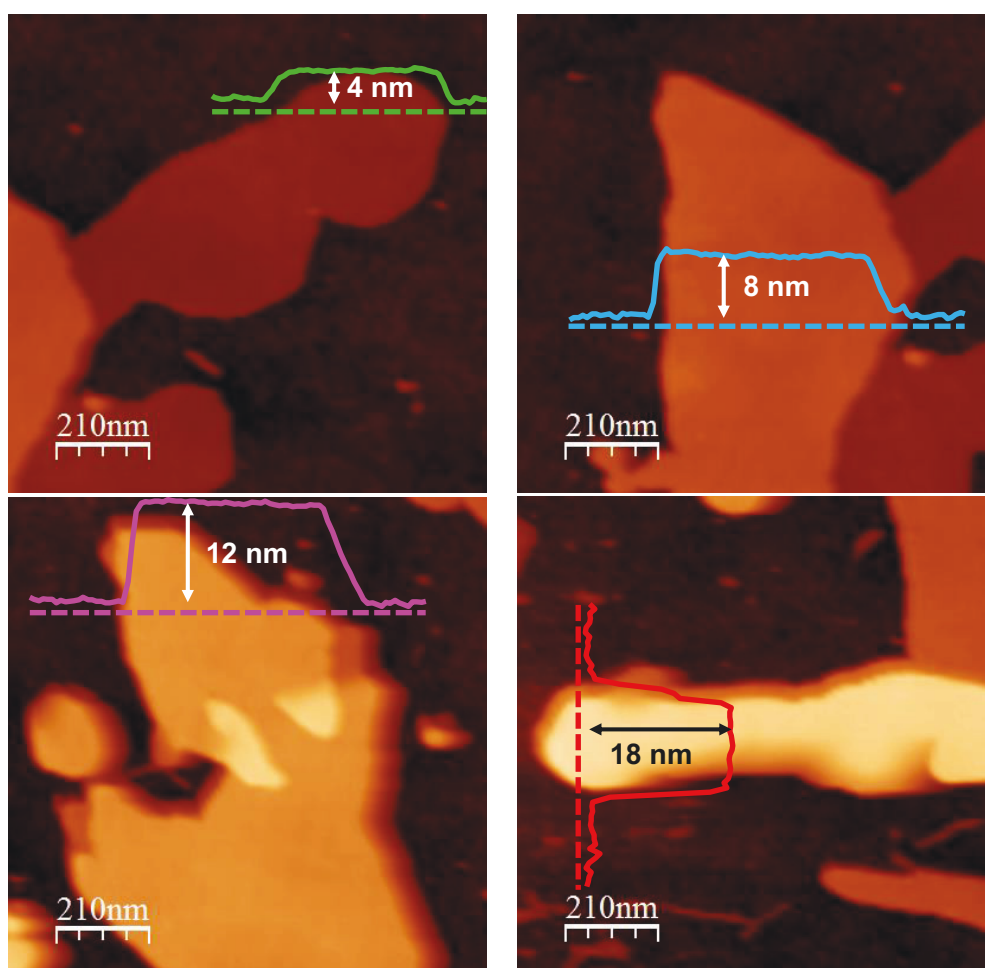


Figure S7. AFM topographic images of different few-layer antimonene flakes. Solid lines correspond to the profiles along the dashed lines, showing step heights multiple of ~ 4 nm.

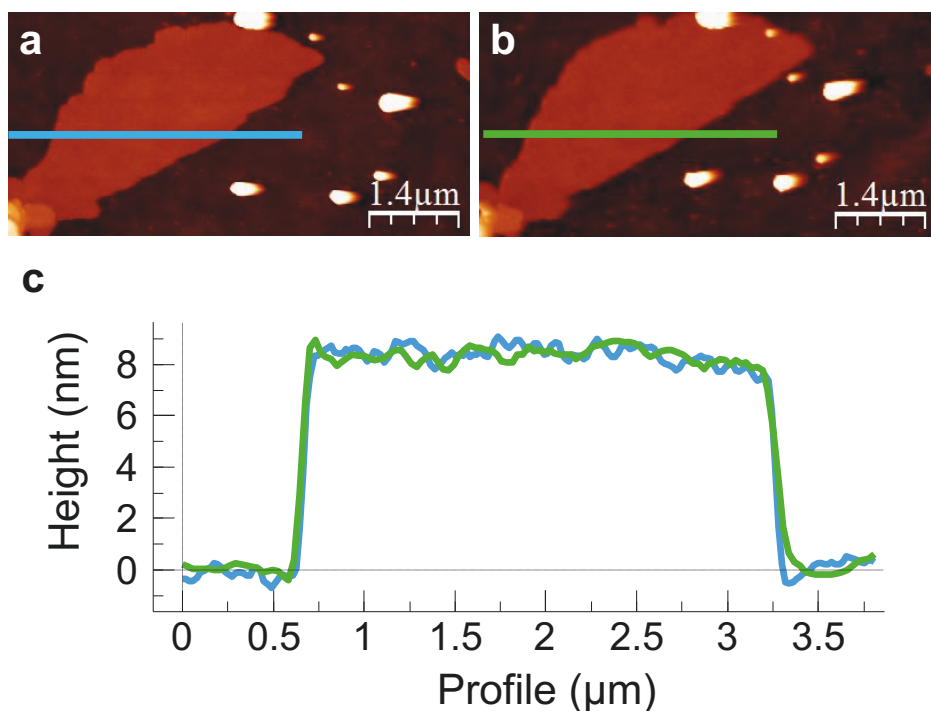


Figure S8. (a) AFM topographic image of a FL antimonene flake taken immediately after exfoliation. (b) Same as in (a) but two weeks later. (c) Profiles taken along the lines drawn in a-b. Please notice the similarity of the corrugation on the antimonene flakes confirming the absence of environmental degradation.

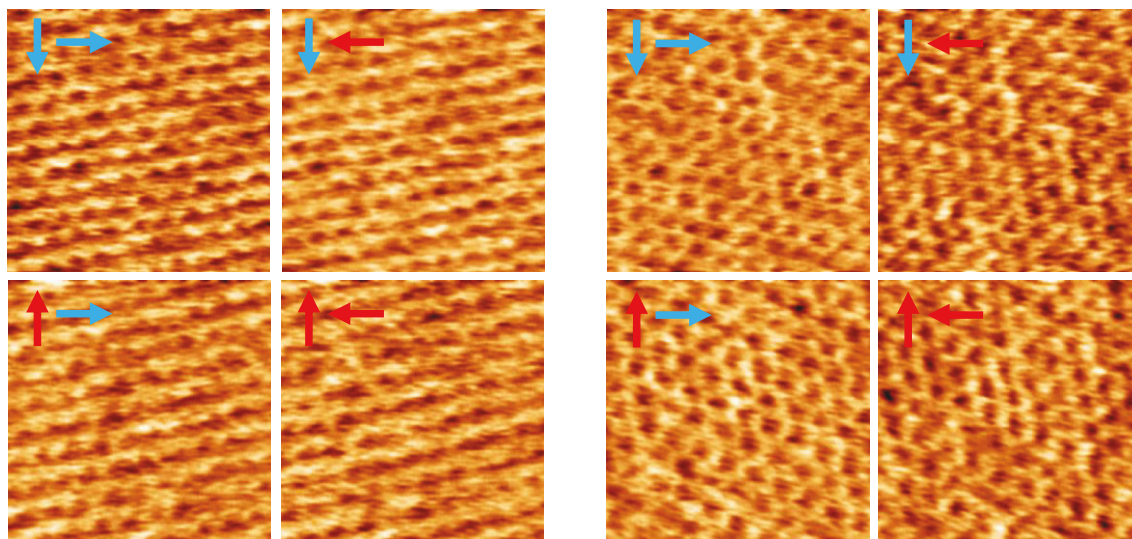


Figure S9. High resolution topographic AFM images corresponding to four consecutive scans on the same 5 x 5 nm² area taken after exposing the sample to atmospheric conditions during more than two weeks. Left and right panels were acquired with scanning angles of 0 and 90 ° respectively. Vertical and horizontal arrows show the direction of the slow and fast scan directions used to acquire each of the images. The observed periodicity is compatible with the antimonene hexagonal atomic lattice.

2.3 Electron Microscopy Studies

2.3.1 Aberration corrected scanning transmission electron microscopy (STEM) combined with electron energy-loss spectroscopy (EELS).

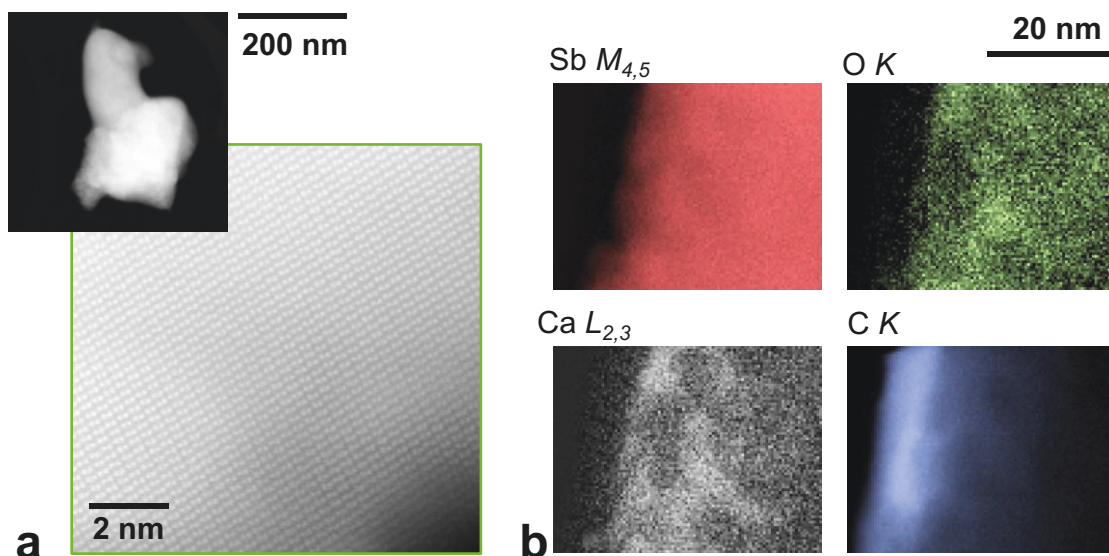


Figure S10. (a) Low magnification HAADF image of a flake (top left) along with an atomic resolution image (image taken along the $[0 -1 2]$ direction). (b) Two dimensional EELS maps acquired near the edge of the flake, exhibiting the signal below the C K (blue), Ca $L_{2,3}$ (gray scale), O K (green) and Sb $M_{4,5}$ (red) absorption edges. Results in (a, b) obtained at 80 kV in a JEOL ARM200cF equipped with a spherical aberration corrector and a Gatan Quantum EEL spectrometer. The LPE method is carried out with 2-propanol that contains 0.2 ppm of Ca according to the information provided by *Panreac*.

2.3.2 Transmission Electron Microscopy (TEM).

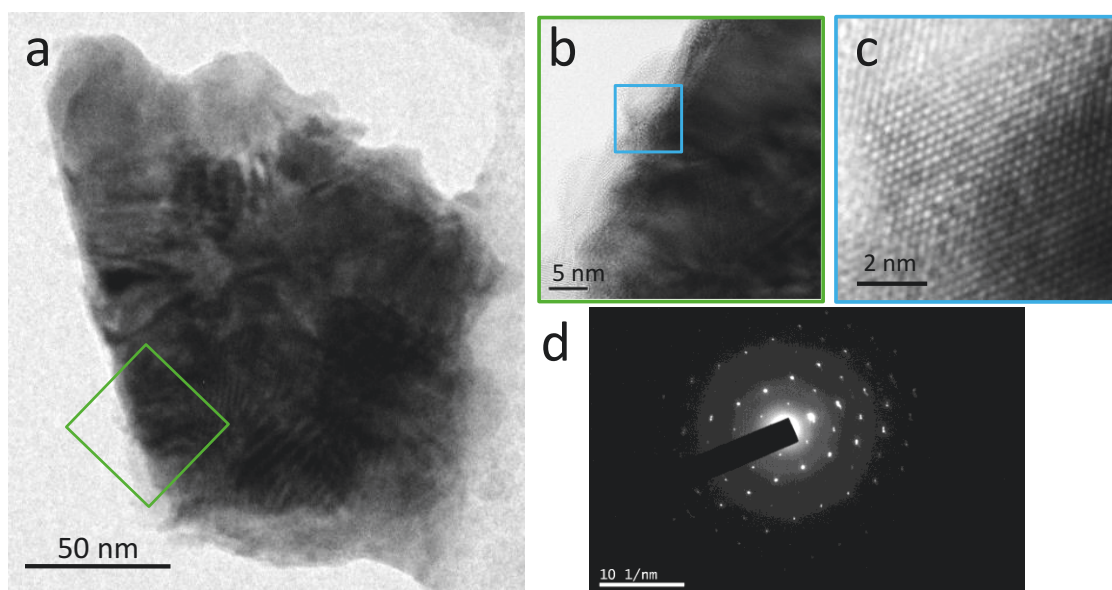


Figure S11. (a) TEM image of a thin antimony flake. (b) Magnification of the green area in (a). (c) Digital magnification of the blue region in (b). (d) Electron diffraction pattern, showing the hexagonal symmetry.

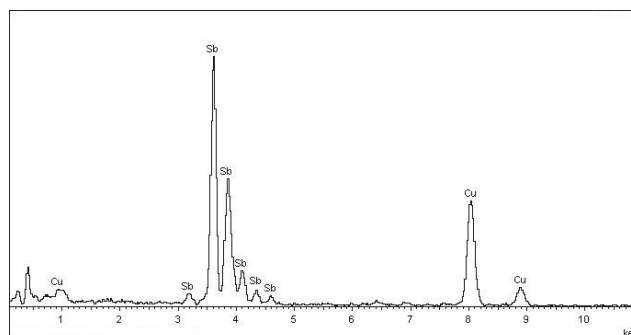


Figure S12. X-Ray Energy Dispersive Spectroscopy (XEDS) microanalysis of few-layer antimonene flakes.

2.4 Raman Spectroscopy

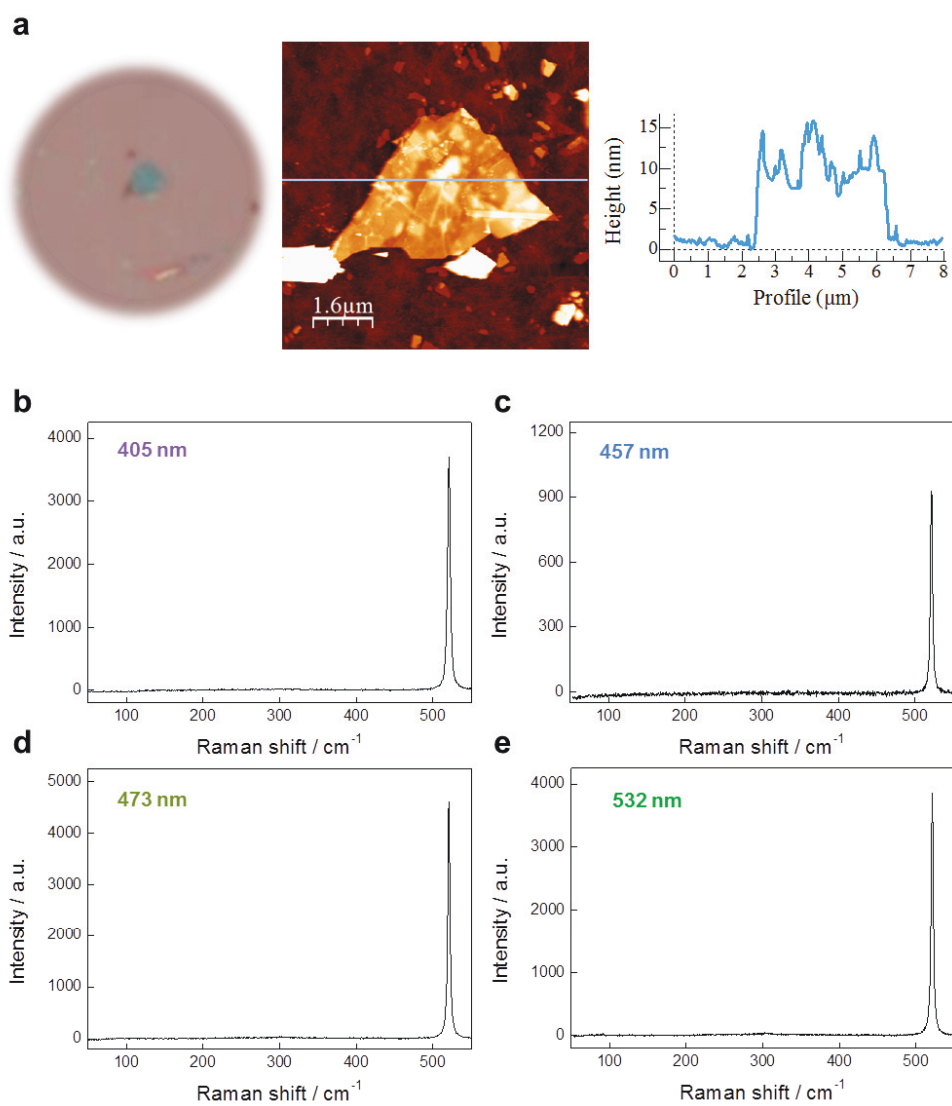


Figure S13. Micromechanically exfoliated flake measured with different laser excitation wavelengths.

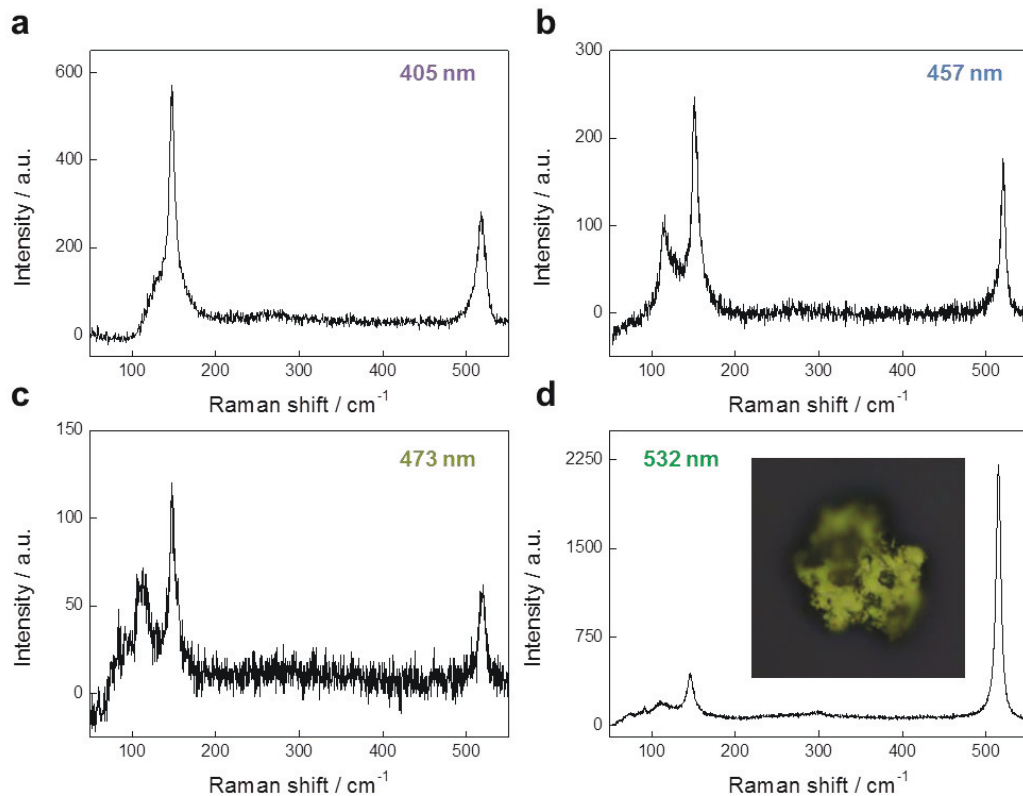


Figure S14. Influence of the laser excitation wavelength on the Raman spectra of bulk antimony.

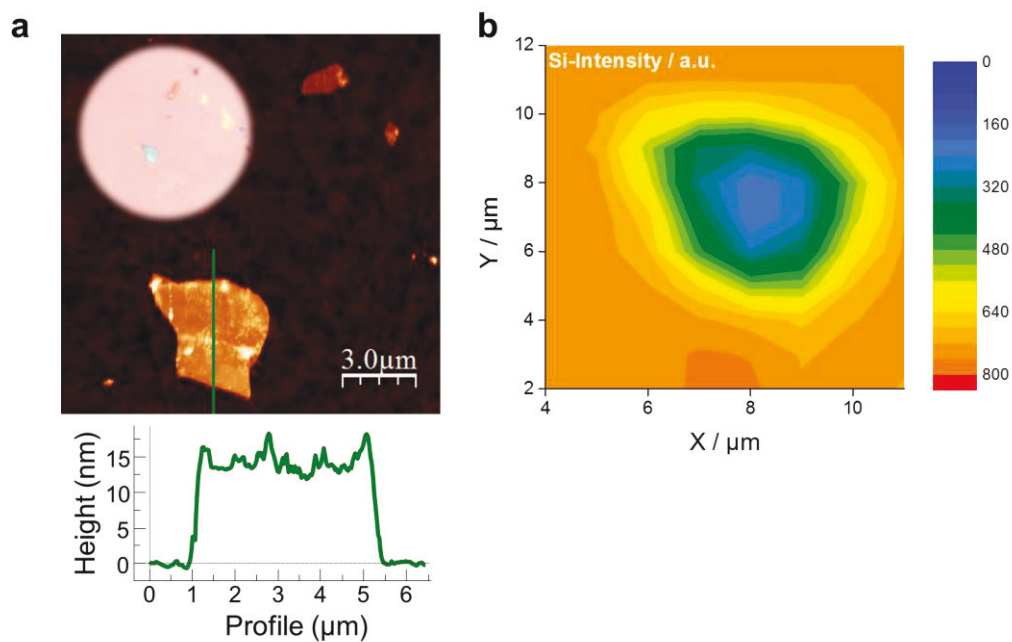


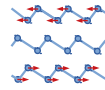
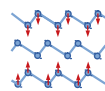
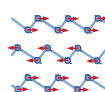
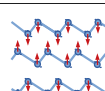
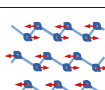
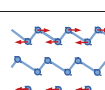
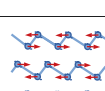
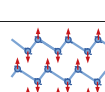
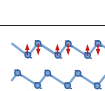
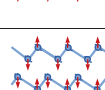
Figure S15. Detection of thin flakes monitoring the Silicon intensity. (a) AFM image of a micrometric flake and its corresponding profile showing a thickness of *ca.* 15 nm. The inset corresponds to the optical micrograph of the same area. (b) Silicon intensity Raman map showing a decrease in the 521 cm^{-1} signal that clearly reveals the morphology of the flake.

2.5 Theoretical calculations

The phonon frequencies at the Γ -point and Raman cross sections were calculated in the frame of density functional perturbation theory on the level of the local-density approximation (LDA) to the exchange-correlation functional as implemented in the Quantum Espresso suite.^[5] We modeled the electron-ion interaction through norm conserving pseudopotentials generated with the ONCVSP package,^[6] where we included the 4d, 5s, and 5p states in the set of valence electrons and applied a cutoff energy of 1200 eV. We used the primitive cells of studied systems, i.e. of hexagonal symmetry in case of the 2D materials and rhombohedral in case of the β -phase of bulk Sb, and fully optimized the atomic positions and the lattice vectors in the periodic directions until the residual forces between atoms were smaller than 0.01 eV/Å. Here, we used ABC stacking for all structures. Interactions of the few-layer systems with residual periodic images due to the 3D boundary conditions were minimized by maintaining a vacuum layer of at least 25 Å. Based on the geometries, we then calculated the Γ -point phonon frequencies and Raman tensors. We used $17 \times 17 \times 1$ ($17 \times 17 \times 17$) Monkhorst-Pack k-point samplings for ground state calculations, geometry optimizations and frequency calculations for the few-layer (bulk) materials. For the Raman calculations, we reduced the grid densities to $14 \times 14 \times 1$ ($14 \times 14 \times 14$), as we were mainly interested in the relative intensities. For the bulk system, the Raman intensities were calculated in the approximation of fixed occupation of the electronic bands, *i.e.* as a semiconductor. The Raman activities shown in Figure 4b of the main text were derived from the calculated Raman tensor under the assumption of backscattering configuration.^[7]

Due to the observed underestimation of the Γ -point calculated frequencies in bulk Sb compared to experiment, we took great care in choosing our method and tested our optimized geometries and phonon frequencies for bulk Sb against several exchange-correlation functionals (LDA, PBE, PBEsol), pseudopotentials and DFT codes employing different basis sets (GPAW, Elk). We thereby ensured consistency and ruled out errors from underconvergence of energies and forces or the pseudopotential approximation. We note that our obtained frequencies deviate from the ones reported recently by Wang *et al.* in Ref. [8]: Using the VASP code, they predict phonon frequencies for bulk Sb that are close to the experimental values of 110 cm⁻¹ and 150 cm⁻¹. On the other hand, the reported frequencies for the three Raman active modes of monolayer Sb are significantly lower than in our calculations. Second, the relative intensities of the E_g and A_{1g} peaks in the simulated Raman spectrum of bulk Sb are opposite to those in our calculations. Unfortunately, we were unable to identify the origin of the deviations based on their reported computational parameters. A contributing factor to the discrepancies might be freezing the semi-core 4d electrons in the employed pseudopotentials/PAWs, which in our experience can change the predicted phonon frequencies in antimony relative to smaller-core pseudopotentials. We believe this underlines the sensitivity of the predicted vibrational properties of Antimony structures to the employed pseudopotential and exchange-correlation approximations and motivates further theoretical studies of the vibrational properties of this material.

Table S1. Calculated phonon frequencies (in cm^{-1}) at the Γ point in few-layer and bulk antimony. The irreducible representations of the symmetry group D_{3d} corresponding to the vibrations is indicated. Rows of the table contain modes with identical displacement pattern for the different layer numbers.^a

	1L	2L	3L	Bulk
	a = 4.01 Å	a = 4.15 Å	a = 4.19 Å	Hex: a = 4.3 Å, c = 11.0 Å Rhomb: a = 4.427 Å, $\varphi = 58.08^\circ$
E_g		45.2	36.2 	
A_{1g}		52.9	40.3 	
E_u			57.6 	
A_{2u}			66.8 	
E_g	166.5 (150 ^b)	149.94	141.2 	88.8 (100 ^b)
E_u		159.11	153.8 	
E_g			156.1 	
A_{1g}	208.3 (195 ^b)	185.3	172.7 	137.4 (148 ^a)
A_{2u}		186.5	181.4 	
A_{1g}			182.0 	

^a Sketches of the calculated displacement patterns of the optical phonon modes are shown for 3L Sb. Analogous to the bilayer structure, the qualitative shape and symmetry of these displacement patterns can be derived from those of the monolayer form (refer to Ref. [9] for a more detailed discussion). The six modes of the 3L structure with highest frequencies show an unintuitive behavior: a larger change in interlayer bond-lengths due to the lattice vibrations leads to a lower frequency. The optimized lattice constants are given for each system. The strong increase of the lattice constants for decreasing layer numbers can be traced back to the nature of the interlayer bonding in antimony, which has a significantly stronger covalent character than the noncovalent bonding in layered materials such as MoS_2 and graphite. The outmost layers thus undergo an atomic rearrangement and contraction due to a lack of bonding partners at the surface; the effect increases with decreasing film thickness. ^b values taken from Ref. [7].

References

- [1] a) I. Horcas, R. Fernández, J. M. Gómez-Rodríguez, J. Colchero, J. Gómez-Herrero, A. M. Baro, *Rev. Sci. Instrum.* **2007**, 78, 013705; b) A. Gimeno, P. Ares, I. Horcas, A. Gil, J. M. Gómez-Rodríguez, J. Colchero, J. Gómez-Herrero, *Bioinformatics* **2015**, 31, 2918-2920.
- [2] P. Nemes-Incze, Z. Osváth, K. Kamarás, L. P. Biró, *Carbon* **2008**, 46, 1435-1442.
- [3] J. N. Coleman, M. Lotya, A. O'Neill, S. D. Bergin, P. J. King, U. Khan, K. Young, A. Gaucher, S. De, R. J. Smith, I. V. Shvets, S. K. Arora, G. Stanton, H. Y. Kim, K. Lee, G. T. Kim, G. S. Duesberg, T. Hallam, J. J. Boland, J. J. Wang, J. F. Donegan, J. C. Grunlan, G. Moriarty, A. Shmeliov, R. J. Nicholls, J. M. Perkins, E. M. Grieveson, K. Theuwissen, D. W. McComb, P. D. Nellist, V. Nicolosi, *Science* **2011**, 331, 568-571.
- [4] M. R. Azani, A. Hassanpour, V. Carcelén, C. Gibaja, D. Granados, R. Mas-Ballesté, F. Zamora, *App. Mater. Today* **2016**, 2, 17-23.
- [5] D P. Giannozzi, S. Baroni, N. Bonini, M. Calandra, R. Car, C. Cavazzoni, D. Ceresoli, G. L. Chiarotti, M. Cococcioni, I. Dabo, A. Dal Corso, S. Fabris, G. Fratesi, S. de Gironcoli, R. Gebauer, U. Gerstmann, C. Gougoussis, A. Kokalj, M. Lazzeri, L. Martin-Samos, N. Marzari, F. Mauri, R. Mazzarello, S. Paolini, A. Pasquarello, L. Paulatto, C. Sbraccia, S. Scandolo, G. Sclauzero, A. P. Seitsonen, A. Smogunov, P. Umari, R. M. Wentzcovitch, *J.Phys. Condens.Matter*, **2009**, 21, 395502.
- [6] D. R. Hamann, *Phys. Rev. B* **2013**, 88, 085117.
- [7] D. Porezag, M.R. Pederson., *Phys. Rev. B* **1996**, 54, 7830.
- [8] G. Wang, R. Pandey, S. P. Karna, *ACS Appl. Matter. Inter.* **2015**, 7, 11490.
- [9] N. Scheuschner, R. Gillen, M. Staiger, J. Maultzsch, *Phys. Rev. B* **2015**, 91, 235409.